



AFRL-OSR-VA-TR-2013-09-1-0308

**ELECTRONIC STRUCTURE AND QUANTUM EFFECTS OF
THIN METAL FILM SYSTEMS BASED ON SILICON CARBIDE**

Tai C. Chiang
University of Illinois at Urbana-Champaign

May 2013
Final Report

DISTRIBUTION A: Approved for public release.

AIR FORCE RESEARCH LABORATORY
AF OFFICE OF SCIENTIFIC RESEARCH (AFOSR)
ARLINGTON, VIRGINIA 22203
AIR FORCE MATERIEL COMMAND

REPORT DOCUMENTATION PAGE					Form Approved OMB No. 0704-0188	
The public reporting burden for this collection of information is estimated to average 1 hour per response, including the time for reviewing instructions, searching existing data sources, gathering and maintaining the data needed, and completing and reviewing the collection of information. Send comments regarding this burden estimate or any other aspect of this collection of information, including suggestions for reducing the burden, to the Department of Defense, Executive Services and Communications Directorate (0704-0188). Respondents should be aware that notwithstanding any other provision of law, no person shall be subject to any penalty for failing to comply with a collection of information if it does not display a currently valid OMB control number.						
PLEASE DO NOT RETURN YOUR FORM TO THE ABOVE ORGANIZATION.						
1. REPORT DATE (DD-MM-YYYY) 24-01-2013		2. REPORT TYPE FINAL REPORT		3. DATES COVERED (From - To) Apr/15/2009-Nov/30/2012		
4. TITLE AND SUBTITLE ELECTRONIC STRUCTURE AND QUANTUM EFFECTS OF THIN METAL FILM SYSTEMS BASED ON SILICON CARBIDE				5a. CONTRACT NUMBER		
				5b. GRANT NUMBER FA9550-09-1-0308		
				5c. PROGRAM ELEMENT NUMBER		
				5d. PROJECT NUMBER		
6. AUTHOR(S) Tai C. Chiang				5e. TASK NUMBER		
				5f. WORK UNIT NUMBER		
7. PERFORMING ORGANIZATION NAME(S) AND ADDRESS(ES) Department of Physics University of Illinois at Urbana-Champaign				8. PERFORMING ORGANIZATION REPORT NUMBER		
9. SPONSORING/MONITORING AGENCY NAME(S) AND ADDRESS(ES) Air Force Office of Scientific Research (AFOSR) 875 N. Randolph St. , Room 3112 Arlington, VA 22203				10. SPONSOR/MONITOR'S ACRONYM(S) AFOSR		
				11. SPONSOR/MONITOR'S REPORT NUMBER(S) AFRL-OSR-VA-TR-2013-0209		
12. DISTRIBUTION/AVAILABILITY STATEMENT DISTRIBUTION A: APPROVED FOR PUBLIC RELEASE						
13. SUPPLEMENTARY NOTES						
14. ABSTRACT This proposal is a study of the electronic structure and quantum effects of layer systems based on hexagonal silicon carbide, a large-gap electronic substrate material suitable for high-power and radiation-resistant applications. High temperature processing of SiC surfaces in vacuum leads to reconstructed surfaces with varying chemical compositions and atomic organizations. Prolonged heating depletes Si from the surface, resulting in the formation of a graphene sheet or a graphite-like structure made of multiple graphene sheets. These systems possess useful and/or unusual electronic structures including Dirac fermion dispersions near the Fermi level for a graphene sheet, band splittings in multiple sheets, and band bending within the SiC. The potential for novel electronic applications has driven large prevailing research efforts within the materials science community. Our research has focused on these low-dimensional systems, the formation of ultrathin metallic overlayers, and the resulting quantum physical properties of the composite systems.						
15. SUBJECT TERMS Electronic structure, graphene, silicon carbide, interfaces						
16. SECURITY CLASSIFICATION OF:			17. LIMITATION OF ABSTRACT		18. NUMBER OF PAGES	
a. REPORT	b. ABSTRACT	c. THIS PAGE	SAR		19a. NAME OF RESPONSIBLE PERSON Tai C. Chiang	
U	U	U			19b. TELEPHONE NUMBER (Include area code) 217-333-2593	

Reset

Final Report

Tai C. Chiang

Abstract

This proposal is a study of the electronic structure and quantum effects of layer systems based on hexagonal silicon carbide, a large-gap electronic substrate material suitable for high-power and radiation-resistant applications. High temperature processing of SiC surfaces in vacuum leads to reconstructed surfaces with varying chemical compositions and atomic organizations. Prolonged heating depletes Si from the surface, resulting in the formation of a graphene sheet or a graphite-like structure made of multiple graphene sheets. These systems possess useful and/or unusual electronic structures including Dirac fermion dispersions near the Fermi level for a graphene sheet, band splittings in multiple sheets, and band bending within the SiC. The potential for novel electronic applications has driven large prevailing research efforts within the materials science community. Our research has focused on these low-dimensional systems, the formation of ultrathin metallic overlayers, and the resulting quantum physical properties of the composite systems. Key discoveries and advances include:

Mapping by angle-resolved photoemission spectroscopy of the spectral functions of graphite and graphene layers at low temperatures reveals a heretofore unreported gap of ~ 67 meV at normal emission. This gap persists to room temperature and beyond, and diminishes for increasing emission angles. We show that this gap arises from electronic coupling to out-of-plane vibrational modes at the K point in the surface Brillouin zone in accordance with conservation laws and selection rules governed by quantum mechanics. Our study suggests a new approach for characterizing phonons and electron-phonon coupling in solids.

Electronic chirality near the Dirac point is a key property of graphene systems. The direction of the isospin vector in monolayer graphene tracks the rotation of the electronic crystal momentum, resulting in a Berry's phase of 180 degrees. By contrast, the isospin in bilayer graphene rotates twice as fast, resulting in a Berry's phase of 360 degrees. We show that these chiral relationships are connected to the spectral intensity patterns as measured by angle-resolved photoemission spectroscopy under different polarization conditions. Specifically, the semicircular patterns at 30 eV for monolayer (bilayer) graphene rotate by $\pm 90^\circ$ ($\pm 45^\circ$) in changing from linearly to circularly polarized light. Calculations confirm that these effects arise from the interplay between electronic chirality and coherent interference of dipole transitions from the s and p polarization components. The measured circular dichroism thus yields definitive information about the phases of the electronic states.

Work has also been carried out to map the phonon dispersion relations of graphene systems over wide regions in the surface Brillouin zone. The quantum electronic structure of metal overlayers is currently under investigation.

Phonon-Induced Gaps in Graphene and Graphite Observed by Angle-Resolved Photoemission

Y. Liu, Longxiang Zhang, M. K. Brinkley, G. Bian, T. Miller, and T.-C. Chiang*

*Department of Physics, University of Illinois at Urbana-Champaign, 1110 West Green Street, Urbana, Illinois 61801-3080, USA,
and Frederick Seitz Materials Research Laboratory, University of Illinois at Urbana-Champaign,
104 South Goodwin Avenue, Urbana, Illinois 61801-2902, USA*

(Received 2 June 2010; published 23 September 2010)

Mapping by angle-resolved photoemission spectroscopy of the spectral functions of graphite and graphene layers at low temperatures reveals a heretofore unreported gap of ~ 67 meV at normal emission. This gap persists to room temperature and beyond, and diminishes for increasing emission angles. We show that this gap arises from electronic coupling to out-of-plane vibrational modes at the \bar{K} point in the surface Brillouin zone in accordance with conservation laws and selection rules governed by quantum mechanics. Our study suggests a new approach for characterizing phonons and electron-phonon coupling in solids.

DOI: 10.1103/PhysRevLett.105.136804

PACS numbers: 73.22.Pr, 71.38.-k, 79.60.Jv

Angle-resolved photoemission spectroscopy (ARPES) is a powerful technique for determining the electronic structure of materials, and it has been applied to numerous systems of scientific and technological interest [1]. The measured spectral functions are related to the quasiparticle self-energies, which are influenced by interactions with elementary excitations including phonons. Electron-phonon coupling is of special interest as it plays a key role in the formation of charge density waves and superconducting states. Its main signature is the “kinks” in dispersion relations near the Fermi level, which have been well documented for a variety of systems including graphene layers of various thicknesses and configurations [2–6]. While strong interest in the electronic structure of these graphitic materials has driven extensive ARPES studies [2,3,7–10], prior work has mostly focused on the quasiparticle band dispersion relations associated with the Dirac cones. Largely unexplored are spectral regions far away from the quasiparticle bands, where direct emission from the quasiparticles is forbidden, but indirect emission through coupling to phonons is allowed. Our work shows that ARPES measurements within the forbidden region can yield valuable information about high-order processes such as electron-phonon coupling. Specifically, the experiment reveals a gap of ~ 67 meV at low temperatures for several graphitic materials including highly oriented pyrolytic graphite (HOPG), natural single-crystal graphite (NSCG), and few-layer graphene (FLG) systems prepared on SiC(0001). A detailed study of the temperature and angular dependences of the gap suggests that the gap arises from out-of-plane vibrational modes at the \bar{K} point, which dominate the coupling to electrons at normal emission.

Our ARPES measurements were performed at the Synchrotron Radiation Center, University of Wisconsin-Madison, using the PGM-A, U-NIM, and Wadsworth beam lines. The energy and momentum resolutions were 20 meV and 0.01 \AA^{-1} , respectively. All spectra were taken with the sample temperature at 60 K, unless otherwise stated. The results from these three samples are similar; this is not

surprising since graphite is essentially a stack of graphene layers weakly bonded together by van der Waals forces.

Figure 1 shows the electronic band structures and phonon dispersion relations for graphite and graphene obtained from first-principles calculations based on the ABINIT program [11–14]. These calculations based on the LDA approximation yield a fairly good overall description of the experiment; more accurate results based on the *GW* approximation are available in the literature [15,16]. The calculated results are very similar for graphene and graphite within the basal plane. The dispersions for graphite are small along the *z* direction (perpendicular to

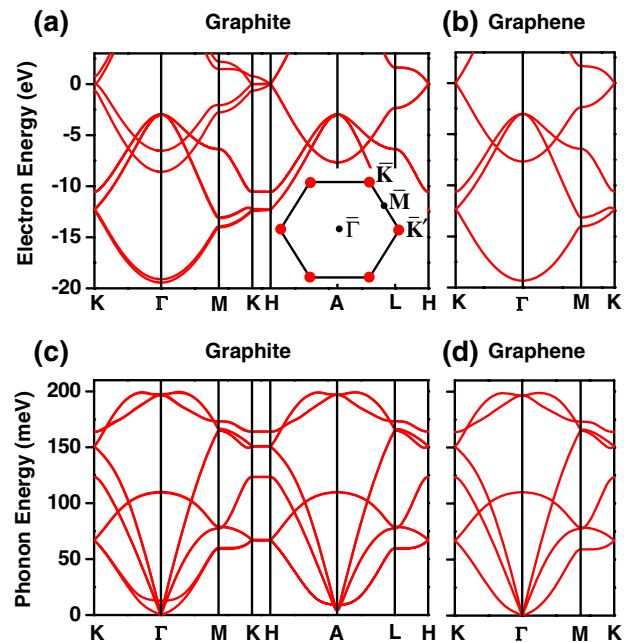


FIG. 1 (color online). Band structures and phonon dispersion relations of graphite (a), (c) and graphene (b), (d) from first-principles calculations. The inset in (a) shows schematically the two-dimensional Fermi surface of graphite and graphene, which consists of 6 Dirac points at \bar{K} and \bar{K}' .

the basal plane). Of special interest are the phonons at the K point of graphene and along K - H in graphite. Their energies are essentially identical. For simplicity, the discussion below will mostly refer to the graphene dispersion relations. Generalization to graphite is straightforward.

The ARPES spectrum at normal emission from HOPG at 60 K [Fig. 2(a)] shows a peak derived from the π band at about -8.5 eV. Emission at angles near the K point [Fig. 2(b)] shows a quasi-Dirac cone from the π band. The random in-plane orientation of graphite crystallites in HOPG dilutes the emission intensity from the Dirac cone, making this feature very weak. Detailed spectra at normal emission and near K [Fig. 2(c)] reveal a gap near the Fermi level at normal emission, as evidenced by a comparison to the spectrum from a reference Ag film. The spectrum at normal emission is very weak as indicated by the relative scales. It actually contains a tiny Fermi edge, which is likely caused by defects [17]. The inset shows the spectrum at normal emission symmetrized about the Fermi level (see supplementary document [18]), which clearly shows a gap of about ± 67 meV in an approximately linear spectrum. This gap, independent of the photon energy, becomes less distinct at higher temperatures [Fig. 2(d)] but remains visible at room temperature. Similar results are obtained from a NSCG [Fig. 2(e)], but there is a somewhat higher background in the gap likely caused by impurities and defects in natural crystals.

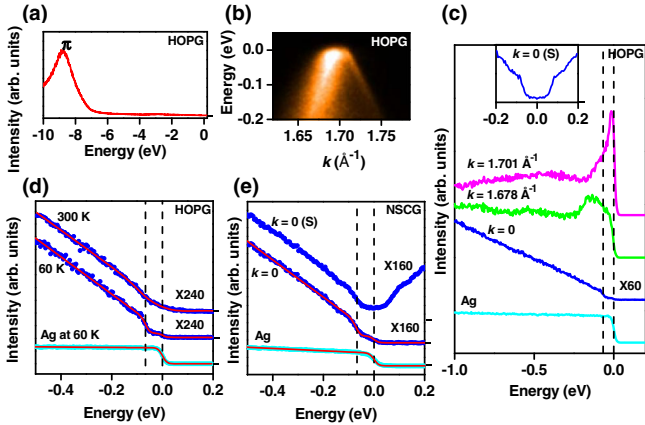


FIG. 2 (color online). ARPES results from HOPG [(a), (b), (c), (d)] and NSCG (e). (a) Normal emission spectrum of HOPG. (b) Measured dispersion of HOPG near \bar{K} along a radial direction pointed away from $\bar{\Gamma}$. (c) Spectra at various in-plane momenta \mathbf{k} for HOPG and a reference spectrum from Ag. The inset is a zoom-in view of the gap near the Fermi level, obtained by symmetrizing (labeled S) the normal emission spectrum with respect to the Fermi level. (d), (e) Comparison between fits (red [medium gray] curves) and normal emission spectra for HOPG (d) and NSCG (e). The vertical dash lines indicate positions of the Fermi level and the edge of the gap. The zero level for each spectrum is indicated by a tick mark on the right vertical axis. The photon energy used was 22 eV. The sample was at 60 K in all cases except for those labeled otherwise.

A similar gap is also observed in FLG. The number of monolayers (MLs) of graphene can be deduced from the Dirac-cone feature near the K point [Fig. 3(a)] [8,9]. Emission from the Si $2p$ core level [Fig. 3(b)] decays rapidly for increasing graphene coverages because of a short photoelectron escape depth [19]. At normal emission, the $6\sqrt{3} \times 6\sqrt{3}$ surface exhibits a broad surface state at about -0.6 eV [Fig. 3(c)] [20]. It becomes an interface state under graphene coverage, and its intensity is attenuated rapidly with increasing graphene coverages. At small graphene coverages, the long tail of the interface state enters into the gap region and interferes with line shape analysis. As a result, the gap is not obvious at 1 ML, but it is quite clear for the thicker graphene layers (2–4 MLs). In each case, there is a metallic Fermi edge, likely due to defects. The gap is clearly seen in the enlarged views of the 3 and 4 ML data and their symmetrized versions [Fig. 3(d)]. Also included is a spectrum for the 3 ML sample near the K point, which shows no gap. The gap feature for the 4 ML case is somewhat weaker, possibly

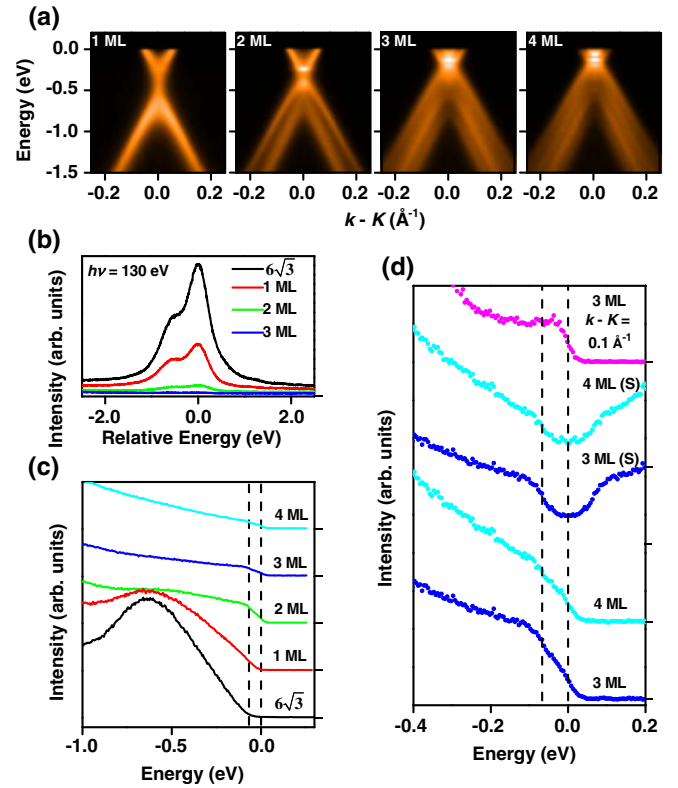


FIG. 3 (color online). ARPES result from FLG on 6H-SiC. (a) Evolution of the Dirac-cone features near the \bar{K} point measured along a direction perpendicular to $\bar{\Gamma}\bar{K}$. (b) Si $2p$ core level. (c) Normal emission spectra as a function of graphene layer thickness. (d) Normal emission spectra and symmetrized versions (labeled S) near the Fermi level for 3 and 4 ML graphene layers. Also shown for comparison is a spectrum near the K point. The zero level for each spectrum is indicated by a tick mark on the right vertical axis. The photon energy used was 50 eV in all cases, except (b) for which 130 eV photons were used.

caused by increased roughness at higher graphene coverages (see [18]) [7].

Because of the large band gap around the Fermi level at the zone center (Fig. 1), the observed gap feature must involve higher order processes. The only states nearby in energy are near the K point. Momentum conservation for normal emission from these states requires the involvement of either an elementary excitation near the K point or a defect. Defect scattering, being strictly energy conserving, cannot account for the gap. Phonon scattering is the only plausible explanation.

The initial state at the K point for graphene is

$$\psi_{\mathbf{K}}(\mathbf{r}) \propto \sum_{\mathbf{R}} \phi(\mathbf{r} - \mathbf{R}) \exp(i\mathbf{K} \cdot \mathbf{R}), \quad (1)$$

where $\phi(\mathbf{r})$ is a carbon p_z orbital, \mathbf{K} is the wave vector at the K point, and the summation is over all lattice vectors \mathbf{R} . The orbital $\phi(\mathbf{r})$ is of even parity within the basal plane. There are actually two degenerate states; the other one involves a p_z orbital centered about the other atom within the unit cell. Photoexcitation of $\psi_{\mathbf{K}}(\mathbf{r})$ leads to

$$\psi'_{\mathbf{K}}(\mathbf{r}) \propto \sum_{\mathbf{R}} \phi'(\mathbf{r} - \mathbf{R}) \exp(i\mathbf{K} \cdot \mathbf{R}), \quad (2)$$

where ϕ' is an excited Wannier function. The excitation involves the usual dipole transition term and a “surface transition” term arising from a nonzero $\nabla \cdot \mathbf{A}$, where \mathbf{A} is the vector potential [21,22]. Both terms are important for three-dimensional systems, but only the dipole term preserves the crystal momentum along z . Graphite is a quasi-two-dimensional crystal with a large perpendicular lattice constant $c = 6.7 \text{ \AA}$ compared to the z extent of the p_z orbital of about $a = 1.4 \text{ \AA}$; the dipole term is scaled down by a factor of $\sim (a/c)^2$. As a result, surface transitions dominate. Since this involves a z -dependent interaction, the in-plane parity of the state is preserved. Thus, ϕ' is also of even parity within the basal plane.

The state $\psi'_{\mathbf{K}}$ can couple via a phonon of wave vector $-\mathbf{K}$ to a state at the zone center:

$$\psi''_0(\mathbf{r}) \propto \sum_{\mathbf{R}} \phi''(\mathbf{r} - \mathbf{R}), \quad (3)$$

where ϕ'' is another excited Wannier function. This state can couple to a plane wave in vacuum, leading to normal emission, if ϕ'' is of even parity within the basal plane [23]. Within the usual rigid-ion approximation, the electron-phonon coupling is

$$\Delta H \propto Q \langle \phi''(\mathbf{r}) | \mathbf{e} \cdot \nabla V(\mathbf{r}) | \phi'(\mathbf{r}) \rangle, \quad (4)$$

where V is the ionic potential, \mathbf{e} is the phonon polarization vector, and Q is the phonon normal mode coordinate. Because both ϕ' and ϕ'' are of even parity within the basal plane, only phonons polarized along z can contribute to this process.

Four phonon modes of graphene at the K point with energies clustered around 150 meV have in-plane polar-

izations (see Fig. 1) [24,25]. The remaining two degenerate phonon modes at energy $E_0 = 67 \text{ meV}$ are polarized along z , and these are the relevant ones. At low temperatures, phonon absorption is quenched. Photoemission assisted by phonon emission should exhibit a gap of 67 meV below the Fermi level E_F by energy conservation. At finite temperatures, the photoemission intensity becomes

$$I(E) \propto (A - BE) \left[F(E - E_F + E_0; T) + \exp\left(\frac{-E_0}{k_B T}\right) F(E - E_F - E_0; T) \right], \quad (5)$$

where F is the Fermi-Dirac distribution function, and the factor $\exp(-E_0/k_B T)$ is the branching ratio between phonon absorption and emission processes. The effective (phonon-assisted) density of states and cross section variations are assumed to be linear (with A and B being constants). At high temperatures, phonon absorption processes could fill in the gap. However, with $E_0/k_B = 770 \text{ K}$, the gap remains visible even at room temperature. The red (medium gray) curves [Fig. 2(d)] are fits to the data at temperatures $T = 60$ and 300 K using Eq. (5) supplemented by a metallic Fermi edge to simulate defect scattering. The fits yield $E_0 = 64 \text{ meV}$, in good agreement with the known value of 67 meV. Analysis of the other cases [e.g., Fig. 2(e)] yields similar values of E_0 within a few meV.

A gap of similar size was reported in a scanning tunneling spectroscopy study of graphene [26,27], and it was attributed to phonon-mediated inelastic tunneling [28]. However, there have been disagreements about the gap size or even the existence of gaps [29–32]. The inconsistencies remain controversial and could be related to sample inhomogeneity, tip structure, or tunneling at the buried interface. The mechanism leading to the ARPES gap does not apply directly to the tunneling case. However, for a well collimated tunneling current perpendicular to the graphene layers from a tip with a simple density of states, the same parity selection rules apply, and a gap of $\sim 67 \text{ meV}$ can be expected.

ARPES is free from tip effects; a further advantage is angular resolution. Experimentally, the gap disappears for increasing emission angle or in-plane momentum [Fig. 4(a)]; the symmetrized spectra are for 3 ML graphene on SiC at 60 K. The two vertical lines indicate the edges of the gap at normal emission. The corresponding first derivatives [Fig. 4(b)] show peaks at the edges of the gap. The gap diminishes and gets filled in for increasing emission angles because phonons at lower wave vectors, and lower energies, become involved.

While the 67 meV phonons are the dominant contributions to the gap at normal emission, other phonons at $\sim 150 \text{ meV}$ are expected to contribute as well, however weakly. The dipole transition term, even though suppressed, is nonzero, and its parity permits the excitation of the in-plane phonons. High-resolution scans indeed

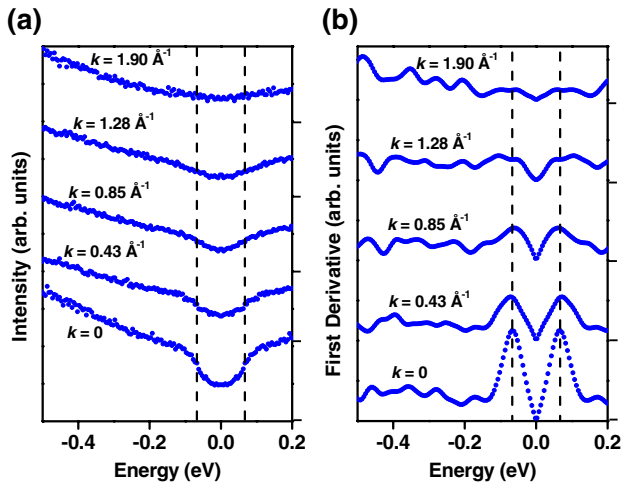


FIG. 4 (color online). Dependence of the gaps on \mathbf{k} . (a) Symmetrized spectra for 3 ML graphene as a function of in-plane momentum \mathbf{k} along the $\bar{\Gamma}\bar{K}$ direction. The photon energy used was 50 eV. (b) Absolute value of the first derivative of (a). The zero level for each spectrum is indicated by a tick mark on the right vertical axis.

show a very weak secondary gap at ~ 150 meV (see [18]). The results suggest the possibility of detailed phonon spectroscopy based on this method.

The present study demonstrates that ARPES spectral regions forbidden for direct emission provide a valuable test ground for detailed investigations of elementary interactions. Electron-phonon coupling is a weak interaction, but its signature shows up clearly because of the absence of other spectral features. This insight is important for a detailed understanding of the basic physics of graphite and graphene [33,34]. Possible applications of the method include phonon spectroscopy and determination of the electron-phonon coupling strength through a detailed analysis of ARPES data. Specifically, the phonon gaps at general points in the Brillouin zone could be used to extract detailed phonon dispersion relations, while the spectral height of each phonon gap provides a direct measure of the electron-phonon coupling strength.

This work is supported by the U.S. Air Force Office of Scientific Research (Grant No. FA9550-09-1-030B). The Synchrotron Radiation Center, where the ARPES work was performed, is supported by the U.S. National Science Foundation (Grant No. DMR-05-37588). We acknowledge the Petroleum Research Fund, administered by the American Chemical Society, and the U.S. National Science Foundation (Grant No. DMR-09-06444) for partial support of the beam line facilities and operations. The NSCG sample was obtained from Chanyong Hwang of the Korea Research Institute of Standards and Science.

*tcchiang@illinois.edu

- [1] S. Hüfner, *Photoelectron Spectroscopy* (Springer-Verlag, New York, 1996), 2nd ed.
- [2] S. Y. Zhou, G.-H. Gweon, and A. Lanzara, *Ann. Phys. (N.Y.)* **321**, 1730 (2006).
- [3] A. Bostwick, T. Ohta, T. Seyller, K. Horn, and E. Rotenberg, *Nature Phys.* **3**, 36 (2007).
- [4] A. Damascelli, Z. Hussain, and Z.-X. Shen, *Rev. Mod. Phys.* **75**, 473 (2003).
- [5] G. Grimvall, *The Electron-Phonon Interaction in Metals* (North Holland, Amsterdam, 1981).
- [6] B. A. McDougall, T. Balasubramanian, and E. Jensen, *Phys. Rev. B* **51**, 13 891 (1995).
- [7] T. Ohta, A. Bostwick, Th. Seyller, K. Horn, and E. Rotenberg, *Science* **313**, 951 (2006).
- [8] S. Y. Zhou *et al.*, *Nature Mater.* **6**, 770 (2007).
- [9] T. Ohta *et al.*, *Phys. Rev. Lett.* **98**, 206802 (2007).
- [10] A. H. Castro Neto, F. Guinea, N. M. R. Peres, K. S. Novoselov, and A. K. Geim, *Rev. Mod. Phys.* **81**, 109 (2009).
- [11] X. Gonze *et al.*, *Comput. Phys. Commun.* **180**, 2582 (2009).
- [12] X. Gonze *et al.*, *Z. Kristallogr.* **220**, 558 (2005).
- [13] X. Gonze, *Phys. Rev. B* **55**, 10 337 (1997).
- [14] X. Gonze and C. Lee, *Phys. Rev. B* **55**, 10 355 (1997).
- [15] M. Lazzeri, C. Attaccalite, L. Wirtz, and F. Mauri, *Phys. Rev. B* **78**, 081406(R) (2008).
- [16] A. Grüneis *et al.*, *Phys. Rev. Lett.* **100**, 037601 (2008).
- [17] N. M. R. Peres, F. Guinea, and A. H. Castro Neto, *Phys. Rev. B* **73**, 125411 (2006).
- [18] See supplementary material at <http://link.aps.org/supplemental/10.1103/PhysRevLett.105.136804>.
- [19] G. Somorjai, *Chemistry in Two Dimensions: Surfaces* (Cornell University Press, Ithaca, 1981).
- [20] K. V. Emtsev, F. Speck, Th. Seyller, L. Ley, and J. D. Riley, *Phys. Rev. B* **77**, 155303 (2008).
- [21] H. J. Levinson, E. W. Plummer, and P. J. Feibelman, *Phys. Rev. Lett.* **43**, 952 (1979).
- [22] T. Miller, W. E. McMahon, and T.-C. Chiang, *Phys. Rev. Lett.* **77**, 1167 (1996).
- [23] J. Hermanson, *Solid State Commun.* **22**, 9 (1977).
- [24] M. Mohr *et al.*, *Phys. Rev. B* **76**, 035439 (2007).
- [25] A. Grüneis *et al.*, *Phys. Rev. B* **80**, 085423 (2009).
- [26] V. W. Brar *et al.*, *Appl. Phys. Lett.* **91**, 122102 (2007).
- [27] Y. Zhang *et al.*, *Nature Phys.* **4**, 627 (2008).
- [28] T. O. Wehling, I. Grigorenko, A. I. Lichtenstein, and A. V. Balatsky, *Phys. Rev. Lett.* **101**, 216803 (2008).
- [29] G. Li, A. Luican, and E. Y. Andrei, *Phys. Rev. Lett.* **102**, 176804 (2009).
- [30] E. Sutter, D. P. Acharya, J. T. Sadowski, and P. Sutter, *Appl. Phys. Lett.* **94**, 133101 (2009).
- [31] P. Lauffer *et al.*, *Phys. Rev. B* **77**, 155426 (2008).
- [32] D. L. Miller *et al.*, *Science* **324**, 924 (2009).
- [33] K. S. Novoselov *et al.*, *Nature (London)* **438**, 197 (2005).
- [34] Y. Zhang, Y.-W. Tan, H. L. Stormer, and P. Kim, *Nature (London)* **438**, 201 (2005).



Visualizing Electronic Chirality and Berry Phases in Graphene Systems Using Photoemission with Circularly Polarized Light

Y. Liu,^{1,2} G. Bian,^{1,2} T. Miller,^{1,2} and T.-C. Chiang^{1,2}

¹*Department of Physics, University of Illinois at Urbana-Champaign, 1110 West Green Street, Urbana, Illinois 61801-3080, USA*

²*Frederick Seitz Materials Research Laboratory, University of Illinois at Urbana-Champaign, 104 South Goodwin Avenue, Urbana, Illinois 61801-2902, USA*

(Received 23 July 2011; published 10 October 2011)

Electronic chirality near the Dirac point is a key property of graphene systems, which is revealed by the spectral intensity patterns as measured by angle-resolved photoemission spectroscopy under various polarization conditions. Specifically, the strongly modulated circular patterns for monolayer (bilayer) graphene rotate by $\pm 90^\circ$ ($\pm 45^\circ$) in changing from linearly to circularly polarized light; these angles are directly related to the phases of the wave functions and thus visually confirm the Berry's phase of π (2π) around the Dirac point. The details are verified by calculations.

DOI: 10.1103/PhysRevLett.107.166803

PACS numbers: 73.22.Pr, 73.20.At, 79.60.-i

Electronic chirality and the Berry's phase are topics of central importance to graphene physics [1–3]. The direction of the isospin vector in monolayer graphene tracks the rotation of the electronic crystal momentum, resulting in a Berry's phase of π [4,5]. By contrast, the isospin in bilayer graphene rotates twice as fast, resulting in a Berry's phase of 2π [6,7]. These unusual phase properties in graphene systems lead to an unconventional quantum Hall effect, which has attracted widespread interest in utilizing graphene as a new platform for electronic applications [1]. Angle-resolved photoemission spectroscopy (ARPES) has been employed extensively to examine the conical band dispersion relations [8,9]. Previous studies of monolayer graphene, using either *s* or *p* polarized light, show that the intensity patterns have a cosine functional form with a maximum along the ΓK direction [9–13]. Another study found that the intensity pattern for bilayer graphene from *s* polarized light has two nodes along the ΓK direction, which can be linked to the Berry's phase [14].

In this work, we employ ARPES with both circularly and linearly polarized light to probe the phase relations of the wave functions. While these relations are already known from simple tight-binding models, the use of circularly polarized light allows direct sensing of the phases in a visual manner. Specifically, the strongly modulated circular patterns for monolayer (bilayer) graphene rotate by $\pm 90^\circ$ ($\pm 45^\circ$) in changing from linearly to circularly polarized light. These angles and directions of rotation are determined by the phase angle of the incident light polarization, and arise from the interplay between electronic chirality and coherent interference of dipole transitions from the *s* and *p* polarization components. The observed ARPES patterns are in excellent agreement with calculations. The phases of electronic wave functions are hard to extract in general, but the information is critical for a number of systems including, apart from graphenes,

topological insulators, complex oxides, and magnetically ordered materials. Our work on graphene layers as model systems demonstrates that photoemission with circularly polarized light is a powerful approach to solve the phase problem.

Our ARPES measurements were performed at the Synchrotron Radiation Center, University of Wisconsin-Madison, using the new U9 VLS-PGM beam line. All spectra were taken with the sample temperature at 60 K. The polarization purity is better than 99% for HP and VP, and better than 80% for LCP and RCP. The accuracy of sample alignment with respect to light polarization is better than 2° . Monolayer and bilayer graphene samples were prepared on the Si-face of a 6H SiC (0001) substrate by graphitization of the surface in an atmosphere of 10^{-6} Torr of disilane to ensure growth of graphene layers with large domain sizes [15,16]. The coverage of graphene layers, excluding the $6\sqrt{3} \times 6\sqrt{3}$ buffer layer, is deduced from the Dirac-cone feature near the *K* point [17–19].

Our ARPES geometry and the coordinate system in relation to the graphene atomic structure and the Brillouin zone are shown in Figs. 1(a)–1(c). Four polarization configurations were employed: horizontal polarization (HP, or *p* polarization), vertical polarization (VP, or *s* polarization), left circular polarization (LCP) and right circular polarization (RCP). The geometry is such that the vector potential **A** of the incident light lies nearly within the sample plane; thus A_z can be ignored to first order. Figure 1(d) shows ARPES results around the *K* point measured along the *y* direction with LCP and RCP. Evidently, photons with different helicity selectively excite one of the two branches of the Dirac cone with opposite isospin directions. The observed difference can be characterized by a dichroism coefficient, *D*, defined as

$$D = \pm(I_4 - I_3)/(I_1 + I_2), \quad (1)$$

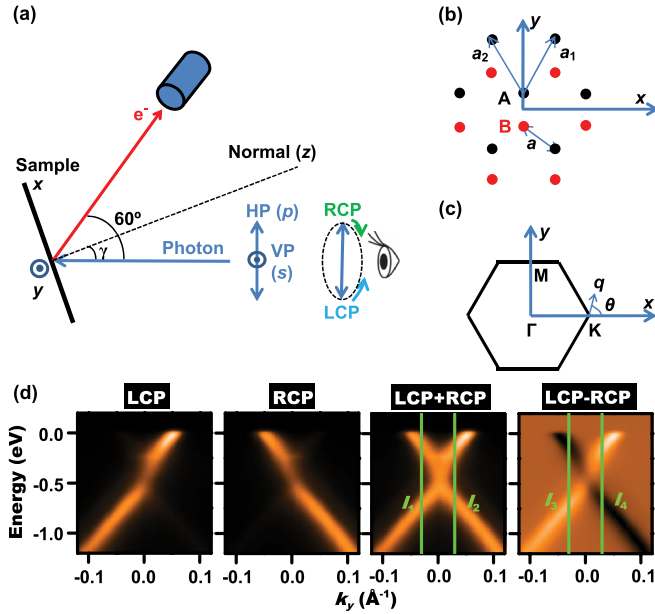


FIG. 1 (color online). Experimental geometry and circular dichroic data. (a) Schematic of experimental setup. HP and VP correspond to p and s polarizations, respectively. Looking toward the sample, LCP (RCP) corresponds to counterclockwise (clockwise) rotation of the electric field vector. (b) Coordinate system relative to the atomic structure of a monolayer graphene. (c) Surface Brillouin zone. \mathbf{q} is wave vector measured from K . (d) Photoemission spectra from monolayer graphene near the K point measured along y using 30 eV photons. The four panels correspond to LCP, RCP, their sum and difference.

where I_1 , I_2 , I_3 , and I_4 are peak intensities of the energy distribution curves as specified in Fig. 1(d), and the $+$ and $-$ signs correspond to the π^* and π bands, respectively. Measurements show that D is close to unity near the K point at 30 eV photon energy. This large dichroic effect results from the different characters of the initial states on the two branches of the Dirac cone; the variations in the photoemission final states are negligible over the narrow range in reciprocal space [20].

Figures 2(a) and 2(b) show typical constant energy maps of the π^* and π bands of monolayer graphene, respectively, using the four polarization configurations. For each band, the semicircular pattern rotates counterclockwise in 90° steps in going from HP to LCP to VP and to RCP. Furthermore, the patterns of the π^* and π bands are related by inversion. The plots on the right-hand side of Fig. 2 show the measured intensity variations of the semicircular arc patterns about the azimuthal angle θ of the wave vector \mathbf{k} relative to the K point [Fig. 1(c)]. The results are well described by cosine functional forms related by 90° offsets. These angular offsets are related to the phase of the initial state wave functions, Ψ_i^k , which are given, to first order, by

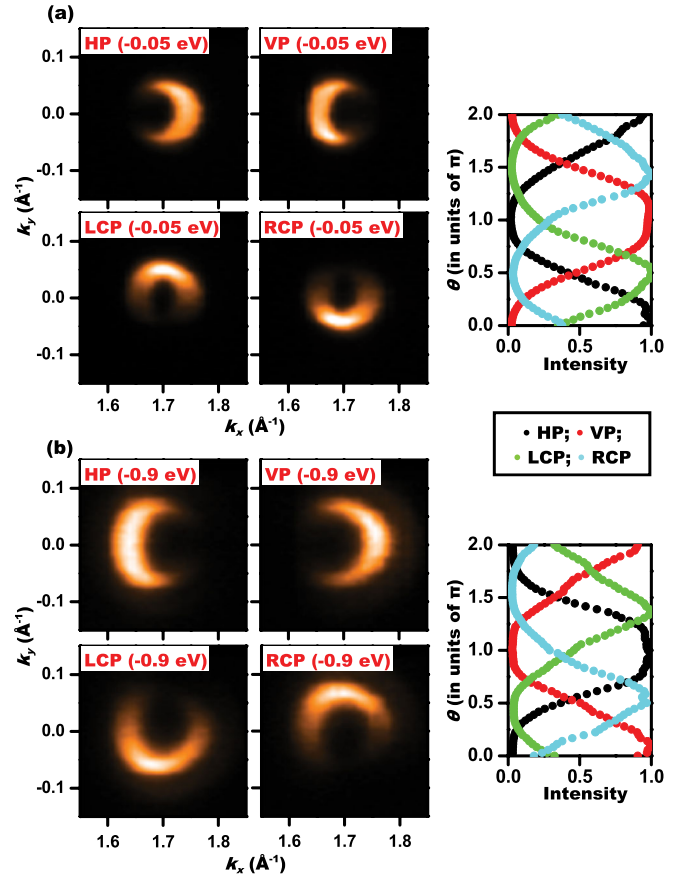


FIG. 2 (color online). ARPES data from monolayer graphene taken with HP, VP, LCP, and RCP using 30 eV photons. The Dirac point is at -0.45 eV. (a) Constant energy maps at -0.05 eV. (b) Constant energy maps at -0.9 eV. The right panels show the intensity of each semicircular arc as a function of θ . Each intensity curve has been normalized to unity maximum intensity.

$$\Psi_i^k(\mathbf{r}) \propto \sum_j \exp(i\mathbf{k} \cdot \mathbf{R}_j) \left[e^{i\theta/2} \phi\left(\mathbf{r} - \mathbf{R}_j - \frac{a}{2}\hat{y}\right) \pm e^{-i\theta/2} \phi\left(\mathbf{r} - \mathbf{R}_j + \frac{a}{2}\hat{y}\right) \right], \quad (2)$$

where \mathbf{R}_j is a lattice vector, ϕ is the carbon p_z orbital, a is the C-C bond length, and the summation is over all lattice vectors. The $+$ and $-$ signs correspond to the π^* and π bands, respectively. The phase factors associated with the two sublattices, $e^{\pm i\theta/2}$, determine the chiral properties of the electronic states and give rise to a Berry's phase of π upon incrementing the azimuthal angle θ by 2π .

The allowed final state of photoemission Ψ_f^k near the K point must be of even parity with respect to reflection about the xz plane. A straightforward calculation yields the photoemission intensities for the π^* and π bands [20]:

$$I \propto |A_x \xi_x (e^{i\theta/2} \pm e^{-i\theta/2}) + A_y \xi_y (e^{i\theta/2} \mp e^{-i\theta/2})|^2$$

$$= \begin{cases} 4\cos^2 \frac{\theta}{2} |A_x|^2 |\xi_x|^2 + 4\sin^2 \frac{\theta}{2} |A_y|^2 |\xi_y|^2 + 4\sin\theta \text{Im}(A_x \xi_x A_y^* \xi_y^*), \\ 4\sin^2 \frac{\theta}{2} |A_x|^2 |\xi_x|^2 + 4\cos^2 \frac{\theta}{2} |A_y|^2 |\xi_y|^2 - 4\sin\theta \text{Im}(A_x \xi_x A_y^* \xi_y^*) \end{cases} \quad (3)$$

where ξ_x and ξ_y are the dipole transition matrix elements for the carbon p_z orbital excited by the x and y components of the vector potential, A_x and A_y , respectively. With $A_y = 0$ for HP and $A_x = 0$ for VP, the first and second terms on the right-hand side of Eq. (3) yield the patterns excited by HP and VP, respectively. The results, proportional to $1 \pm \cos(\theta)$, are in good agreement with experiment [13]. However, the results are independent of the sign of θ . A transformation $\theta \rightarrow -\theta$ reverses the phases of the chiral electronic states [Eq. (2)], but leaves the intensity patterns invariant. Thus, measurements based on HP and VP alone are insufficient to fully determine the chiral phase relationships.

This indetermination can be resolved by using circularly or elliptically polarized light, for which the third term on the right-hand side of Eq. (3) comes into play. This term contains a factor of $\sin(\theta)$, an odd function of θ ; thus, these measurements should uniquely specify the sense of θ . At 30 eV, $\xi_x \approx \xi_y$ as will be shown below. With A_x being real and A_y being imaginary for elliptical polarization, the photoemission intensity is reduced to

$$I \propto 2|\xi_x|^2 A_0^2 [1 \pm \cos(\theta + 2\chi)], \quad (4)$$

where $A_0^2 = |A_x|^2 + |A_y|^2$ and $\chi = \arg(A_x + A_y)$ is the phase angle of the light polarization. Equation (4) shows that the intensity patterns have the same cosine forms as the case of linear polarization except for an angular offset of 2χ , or twice the phase angle of the elliptical polarization. A nonzero offset removes the sign ambiguity of θ ; and the patterns become asymmetric with respect to the transformation $\theta \rightarrow -\theta$. With $\chi = -\pi/4, 0, \pi/4$ and $\pi/2$ for LCP, HP, RCP, and VP, respectively, the patterns should rotate clockwise in 90° steps following this sequence, which is indeed observed experimentally (Fig. 2). The third term in Eq. (3), resulting from interference between the dipole transitions excited by A_x and A_y , uniquely determines the direction of rotation.

The chirality of bilayer graphene is another interesting test case. The Dirac cone is split into two pieces. For the main cone at the Dirac point, the phase factors $e^{\pm i\theta/2}$ in Eq. (2) are replaced by $e^{\pm i\theta}$. Thus, the isospin rotates twice as fast as the monolayer case [7]. As a result, the intensity patterns become “compressed” by a factor of 2 as a function of θ . The single intensity maximum for the monolayer case for each polarization configuration becomes two intensity maxima separated by 180° . The angular offset for the different polarization configurations should become one half of the monolayer case, or 45° . Specifically, the two intensity maxima should be located at $\theta_{\max} = \mp\chi, \mp\chi + \pi$, with the $-$ and $+$ signs corresponding to the

π^* and π bands, respectively. This is indeed seen in the experiment [Fig. 3(a)]. Because of the splitting of the Dirac cones, the photoemission intensity described by Eq. (4) should additionally be modified to include this effect [20]. This explains the other details of the data and why the intensity maximum at $\theta = \pi$ for HP appears missing [14,21]. Figure 3(b) shows the calculated intensity patterns, which agree well with the experiment. The characteristic 45° rotations of the intensity patterns between linear and circular polarizations, as well as the angular positions of the intensity maxima, are direct consequences

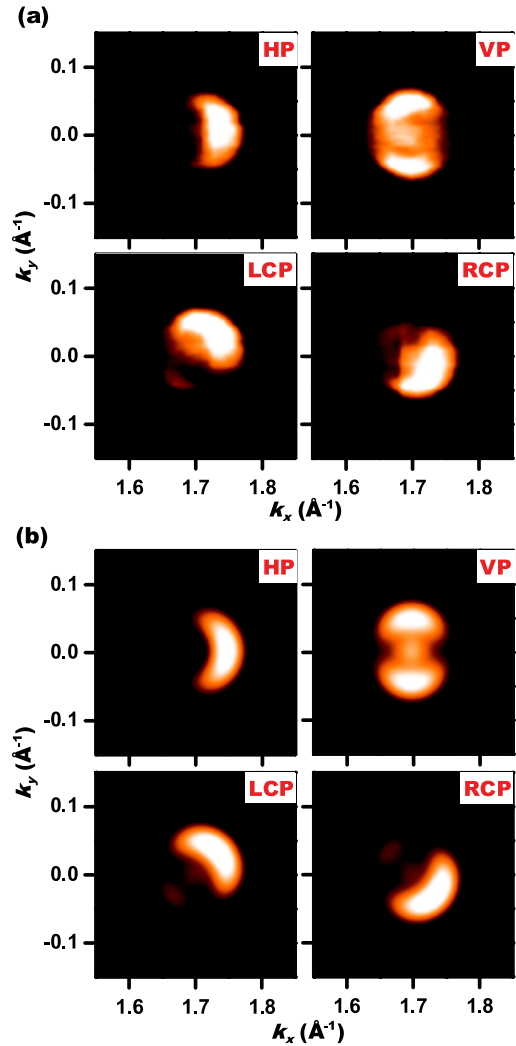


FIG. 3 (color online). ARPES data from bilayer graphene taken with HP, VP, LCP, and RCP using 30 eV photons. The Dirac point is at -0.3 eV. (a) Constant energy maps at -0.05 eV. (b) Calculated results with a Gaussian broadening of $\sigma = 0.015 \text{ \AA}^{-1}$ in k space.

of the electronic chirality and a Berry's phase of 2π in bilayer graphene (vs. π in monolayer graphene).

The interference term in Eq. (3) depends on the phase difference between ξ_x and ξ_y . Let

$$\lambda e^{i\beta} = \xi_y / \xi_x, \quad (5)$$

where λ and β are the amplitude ratio and phase difference, respectively, which can both depend on the photon energy because of variations in the final state. The amplitude ratio λ can be extracted from the intensity ratio ($=\lambda^2$) between VP and HP at $\theta = \pm\pi/2$ [Fig. 4(a)]. The phase difference β can be extracted from the measured dichroism coefficient D [Fig. 4(b)] via

$$\beta = \cos^{-1}\left(\frac{D(1 + \lambda^2)}{2\lambda}\right). \quad (6)$$

The deduced β [Fig. 4(c)] is close to zero for photon energies above 30 eV, but increases at lower photon

energies, where final-state band structure effects become significant [20,22]. Our results show that $\xi_x = \xi_y$ is well satisfied at 30 eV, which leads to very simple pattern rotations seen in Figs. 2 and 3. At high photon energies, band structure effects for the photoemission final states diminish, and we expect $\lambda \rightarrow 0$ and $\beta \rightarrow 0$ based on symmetry considerations [20]. However, an additional contribution from surface photoemission can come into play at very high photon energies [20,23–25], and the analysis can become more involved.

Our study thus shows that polarization-dependent ARPES can be a powerful tool for probing the phases of electronic wave functions in solids. While circular dichroic effects are well known in gas phase ARPES [26–28], much less has been studied for solid-state systems because of complications including electron correlation [29,30]. The Dirac Fermions in graphene systems are of special interest because of their chirality and nontrivial Berry's phases, which can be conveniently probed by elliptically polarized light with a built-in rotation of the vector field. Interference of the dipole transitions gives rise to the observed pattern rotations governed by the ellipticity of the incident light. This understanding and the methodology presented here should be useful for exploring other systems and problems including topological insulators, spin splittings and magnetic ordering. In particular, the surface states on topological insulators should have a nontrivial Berry's phase, and a recent photoemission study indeed revealed interesting circular dichroic effects [31,32]. Further analysis of the topological states based on the present method is underway.

Y. L. thanks C. Hwang for helpful discussion. This work is supported by the U.S. Air Force Office of Scientific Research (grant FA9550-09-1-030B). The Synchrotron Radiation Center, where the ARPES work was performed, is supported by the U.S. National Science Foundation (grant DMR-05-37588). We acknowledge the Petroleum Research Fund, administered by the American Chemical Society, and the U.S. National Science Foundation (grant DMR-09-06444) for partial support of the beam line facilities and operations.

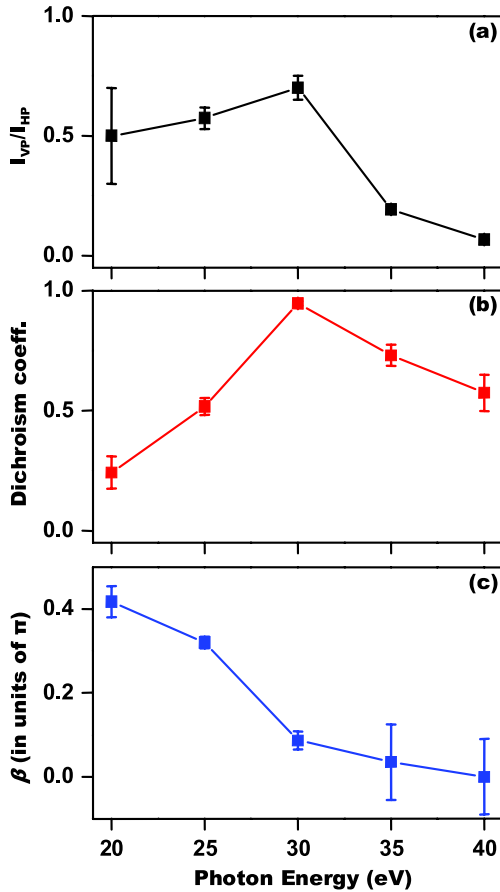


FIG. 4 (color online). Deduction of the phase difference β for monolayer graphene. (a) The photoemission intensity ratio ($=\lambda^2$) between VP and HP at ± 0.4 eV relative to the Dirac point as a function of photon energy. The “error bars” indicate the differences between results for the π^* and π bands. (b) The corresponding dichroism coefficient, D , obtained similarly. (c) The deduced phase difference (β) between transition matrix elements from HP and VP.

- [1] A. H. Castro Neto, F. Guinea, N. M. R. Peres, K. S. Novoselov, and A. K. Geim, *Rev. Mod. Phys.* **81**, 109 (2009).
- [2] M. I. Katsnelson, K. S. Novoselov, and A. K. Geim, *Nature Phys.* **2**, 620 (2006).
- [3] M. V. Berry, *Proc. R. Soc. A* **392**, 45 (1984).
- [4] K. S. Novoselov *et al.*, *Nature (London)* **438**, 197 (2005).
- [5] Y. Zhang, Y.-W. Tan, H. L. Stormer, and P. Kim, *Nature (London)* **438**, 201 (2005).
- [6] K. S. Novoselov *et al.*, *Nature Phys.* **2**, 177 (2006).
- [7] E. McCann and V. I. Fal’ko, *Phys. Rev. Lett.* **96**, 086805 (2006).

- [8] S. Y. Zhou *et al.*, *Nature Phys.* **2**, 595 (2006).
- [9] A. Bostwick, T. Ohta, T. Seyller, K. Horn, and E. Rotenberg, *Nature Phys.* **3**, 36 (2006).
- [10] E.L. Shirley, L.J. Terminello, A. Santoni, and F.J. Himpsel, *Phys. Rev. B* **51**, 13 614 (1995).
- [11] M. Mucha-Kruczyński *et al.*, *Phys. Rev. B* **77**, 195403 (2008).
- [12] A. Bostwick *et al.*, *Prog. Surf. Sci.* **84**, 380 (2009).
- [13] I. Gierz, J. Henk, H. Höchst, C. R. Ast, and K. Kern, *Phys. Rev. B* **83**, 121408(R) (2011).
- [14] C. Hwang *et al.*, *Phys. Rev. B* **84**, 125422 (2011).
- [15] J. Hass, W.A. de Heer, and E.H. Conrad, *J. Phys. Condens. Matter* **20**, 323202 (2008).
- [16] R.M. Tromp and J.B. Hannon, *Phys. Rev. Lett.* **102**, 106104 (2009).
- [17] S. Y. Zhou *et al.*, *Nature Mater.* **6**, 770 (2007).
- [18] T. Ohta *et al.*, *Phys. Rev. Lett.* **98**, 206802 (2007).
- [19] Y. Liu *et al.*, *Phys. Rev. Lett.* **105**, 136804 (2010).
- [20] See Supplemental Material at <http://link.aps.org/supplemental/10.1103/PhysRevLett.107.166803> for additional data and details of the calculations.
- [21] T. Ohta, A. Bostwick, T. Seyller, K. Horn, and E. Rotenberg, *Science* **313**, 951 (2006).
- [22] H. Ohsawa *et al.*, *Solid State Commun.* **61**, 347 (1987).
- [23] H. J. Levinson, E. W. Plummer, and P. J. Feibelman, *Phys. Rev. Lett.* **43**, 952 (1979).
- [24] T. Miller, W.E. McMahon, and T.-C. Chiang, *Phys. Rev. Lett.* **77**, 1167 (1996).
- [25] V.B. Zabolotnyy *et al.*, *Phys. Rev. B* **76**, 024502 (2007).
- [26] S. Motoki *et al.*, *Phys. Rev. Lett.* **88**, 063003 (2002).
- [27] T. Jahnke *et al.*, *Phys. Rev. Lett.* **88**, 073002 (2002).
- [28] D. Doweck *et al.*, *Phys. Rev. Lett.* **104**, 233003 (2010).
- [29] A. Kaminski *et al.*, *Nature (London)* **416**, 610 (2002).
- [30] D. V. Vyalikh *et al.*, *Phys. Rev. Lett.* **100**, 056402 (2008).
- [31] M.Z. Hasan, *Physics* **3**, 62 (2010).
- [32] Y.H. Wang *et al.*, *arXiv:1101.5636v1*.